Univerzita Karlova v Praze
Matematicko-fyzikální fakulta

BAKALÁŘSKÁ PRÁCE

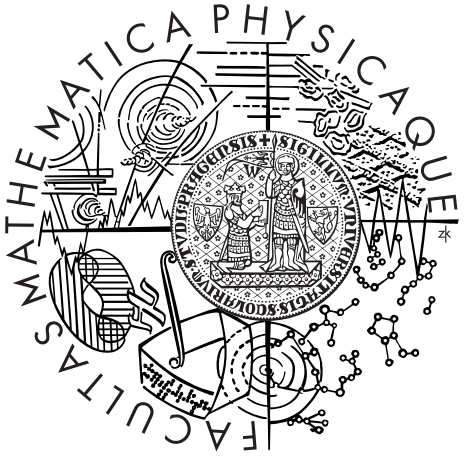

Károly Marák

Optika periodických nanostruktur

Fyzikální ústav UK

Vedoucí bakalářské práce: RNDr. Martin Veis, Ph.D.
Studijní program: Fyzika
Studijní obor: Obecná fyzika

Praha 2013

Charles University in Prague
Faculty of Mathematics and Physics

BACHELOR THESIS

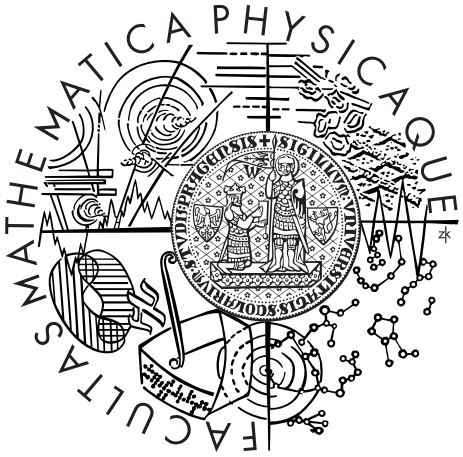

Károly Marák

Optics of periodic nanostructures

Institute of Physics of Charles University

Supervisor of the bachelor thesis: RNDr. Martin Veis, Ph.D.
Study programme: Physics
Specialization: General Physics

Prague 2013

I dedicate this thesis to my brother who was able to help me suffer through the technical miseries of TeX and Mathematica.

I declare that I carried out this bachelor thesis independently, and only with the cited sources, literature and other professional sources.

I understand that my work relates to the rights and obligations under the Act No. 121/2000 Coll., the Copyright Act, as amended, in particular the fact that the Charles University in Prague has the right to conclude a license agreement on the use of this work as a school work pursuant to Section 60 paragraph 1 of the Copyright Act.

In ..... date ..... signature of the author

Název práce: Optika periodických nanostruktur

Autor: Károly Marák

Katedra: Fyzikální ústav UK

Vedoucí bakalářské práce: RNDr. Martin Veis, Ph.D., Fyzikální ústav UK

Abstrakt: Periodické nanostruktury, jako jsou difrakční mřížky, jsou hojně využívány ve fotonických zařízeních, a nově i v solárních článcích. Neustále se rozvíjející technologie jejich výroby vyžadují rovněž zdokonalování charakterizačních technik. V této práci je představena modální metoda popisu optické odezvy anizotropních difrakčních mřížek. Na základě této metody je vytvořen numerický model. Správnost modelu je nejprve ověřena na jednoduchém příkladu Fabry-Perotova rezonátoru, kde spočtené hodnoty reflektivity odpovídají analytické teorii. Poté byla představena struktura solarního článku s difrakční mřížkou. Paramatery této mřížky byly optimalizovány pro co největší účinnost pohlcení světelné vlny. Nakonec byl numerický model použit pro výpočet magnetooptické odezvy permalloyové difrakční mřížky. Bylo ukázáno, že parametry mřížky získané při výrobě neodpovídají reálným hodnotám.

Klíčová slova: difrakční mřížky, magnetooptická spektroskopie, spektroskopická elipsometrie, solární články

Title: Optics of periodic nanostructures

Author: Károly Marák

Department: Institute of Physics of Charles University

Supervisor: RNDr. Martin Veis, Ph.D., Institute of Physics of Charles University

Abstract: Periodic nanostructures, such as diffraction gratings, are widely used in photonic devices and recently in solar cells. Rapidly developing technologies of their preparation require improvements of characterization methods. In this thesis, the model method for the description of optical response of anisotropic diffraction gratings is introduced. This method is used to create a numerical model. The correctness of this model is verified on the basic example of the Fabry-Perot resonator, where the numerically calculated values of reflectivity correspond with the analytical ones. Afterwards, a new structure of a solar cell with diffraction grating was introduced. Parameters of this grating were optimized to obtain to highest efficiency of light trapping inside the solar cell. Finally, the optical and magneto-optical response of permalloy grating was calculated. It was found, that the factory parameters of the grating do not correspond with real values.

Keywords: diffraction gratings, magneto-optical spectroscopy, spectroscopic ellipsometry, solar cells

Contents

Chapter 1

Introduction

1.1 Diffraction Gratings

Diffraction gratings have been used in spectroscopy and other studies of electromagnetic phenomena for nearly two centuries. Josef Fraunhofer (1798-1826), the discoverer of the dark lines in the solar spectrum, built the first gratings om 1819 by winding fine wires around two parallel screws [1]. However, it is only during the past forty years or so that a thorough understanding of nearly all aspects of the behavior of diffraction gratings has been archived through the consistent application of Maxwell's equations with the help of advanced analytical and numerical techniques.

Simply said, a diffraction grating is an optical component with a periodic structure used to split and diffract light into beams traveling in different directions. Because these directions depend on the frequency of the incident electromagnetic wave, it can be used as a dispersive element. Because of this, gratings are often used in monochromators and spectrometers.

Modern gratings may have up to thousands of lines per millimeter with near-perfect periodicity. The groove shapes can be controlled to be sinusoidal, rectangular (as shown in fig.1.1) and so forth; these gratings can be made on various metal, plastic and glass substrates and coated with thin-film metal or dielectric stacks. The primary applications of diffraction gratings are in spectroscopy (where they are used for analyzing the frequency content of electromagnetic radiation), but they

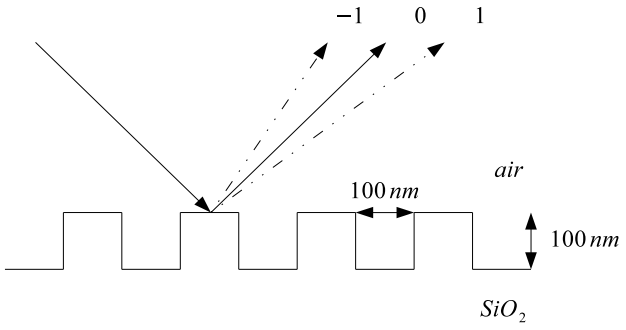

Figure 1.1: Cross section of a simple rectangular grating made of SiO_2, with three orders of the reflected light displayed

are also used as wavelength selectors in tunable lasers, beam sampling mirrors in high-power lasers, band-pass filters, pulse compressors and polarization-sensitive optics, among other applications.

1.1.1 Grating Theories

There are several theoretical approaches dealing with the EM theory of gratings. The simplest theory of gratings treats them as corrugated structures that modulate the amplitude and/or phase of the incident beam in proportion to the local reflectivity and the height or depth of the surface relief features. The modulated reflected (or transmitted) wavefront is then decomposed into its Fourier spectrum to yield the various diffracted orders. Known as the scalar theory of gratings, this elementary treatment yields the correct number and direction of propagation for the diffracted orders, but it does not provide an accurate estimate of the amplitude, phase and polarization state of each order.

From a mathematical point of view, Maxwell's equations can be expressed as partial differential equations. In the grating case, they have constant coefficients - they can be solved numerically in two dimensions. Because of numerical instabilities, this method - the classical differential method - only works for shallow gratings.

Modal methods, like the one we're describing in this work, work for lamellar profiles. They are based on the decomposition of EM field in a combination of modes, which are some base vectors chosen according to the situation.

The integral method is based on the idea that the solution of electromagnetic scattering problems can be found by simple integration, provided that the field and its normal derivative on the surface of the scattering object (and at infinity) are known.

The finite-element method represents the field as a sum of elementary functions ϕ_i over the mesh cells number:

$$E = \sum c_m \phi_m(x, y), \tag{1.1}$$

with $c_m$being the unknown amplitudes. ϕ_m is assumed to be different from zero only in the m-th cell.

See Table 1.1 for a summary of calculation methods.

For more details about the methods used to describe diffraction gratings, see [2].

Table 1.1: A summary of calculation methods

Method	TE polarization	TM polarization	Special media	Computation time and memory requirements	Problems
Volume finite-element	independent	independent	easy	very large	meshing
Surface finite-element	independent	independent	difficult	moderate	programming, singularities
Classical integral	independent	independent	difficult	moderate	programming, singularities
Fictious sources	independent	independent	difficult	moderate	meshing
Classical differential	O. K.	problems	easy	short for TE and/or dielectrics	TM case due to jump of E_x
Moharam & Gaylord	O. K.	problems	more difficult but realistic	short for TE and/or dielectrics	TM case due to jump of E_x. Staircase representation of the profile for short Λ/d
Modal	independent	independent	difficult	short	Staircase representation of the profile for short Λ/d
Conformal mapping	independent	independent	difficult	short	Difficult mapping
Method of Chandezon	independent	independent	difficult (has to be combined with numerical integration)	short	Differentiable profile (not very steep). Not too many diffraction orders.
Rayleigh method	independent	independent	easy	short	Shallow grooves without edges.

Chapter 2

Electromagnetic Waves in Periodic Media

2.1 Maxwell's Equations and the Wave Equation

Maxwell's equations are a set of partial differential equations that describe how electric and magnetic fields are generated .In the absence of macroscopic currents, charges, polarization or magnetization the equations have the following form[1]:

$$\nabla.\mathbf{E} = 0, \tag{2.1}$$

$$\nabla.\mathbf{B} = 0, \tag{2.2}$$

$$\nabla \times \mathbf{E} = -\frac{\partial \mathbf{B}}{\partial t}, \tag{2.3}$$

$$\nabla \times \mathbf{B} = \overleftrightarrow{\boldsymbol{\mu}}.\overleftrightarrow{\boldsymbol{\epsilon}}.\frac{\partial \mathbf{E}}{\partial t}. \tag{2.4}$$

Here $\mathbf{E}$ is the electric field vector, $\mathbf{B}$ is the magnetic field vector, $\overleftrightarrow{\boldsymbol{\mu}}$is the permeability tensor and $\overleftrightarrow{\boldsymbol{\epsilon}}$is the permittivity tensor. From these equations, we can derive the so-called wave equation, which desribes the propagation of electromagnetic waves:

$$\Delta\mathbf{E} - \overleftrightarrow{\boldsymbol{\mu}}.\overleftrightarrow{\boldsymbol{\epsilon}}.\frac{\partial^2 \mathbf{E}}{\partial t^2} = 0. \tag{2.5}$$

2.2 Polarization

One solution to Maxwell's equations is a monochromatic plane wave:

$$\mathbf{E} = \mathbf{E_0} e^{\imath(\mathbf{k}.\mathbf{r}-\omega t)}, \tag{2.6}$$

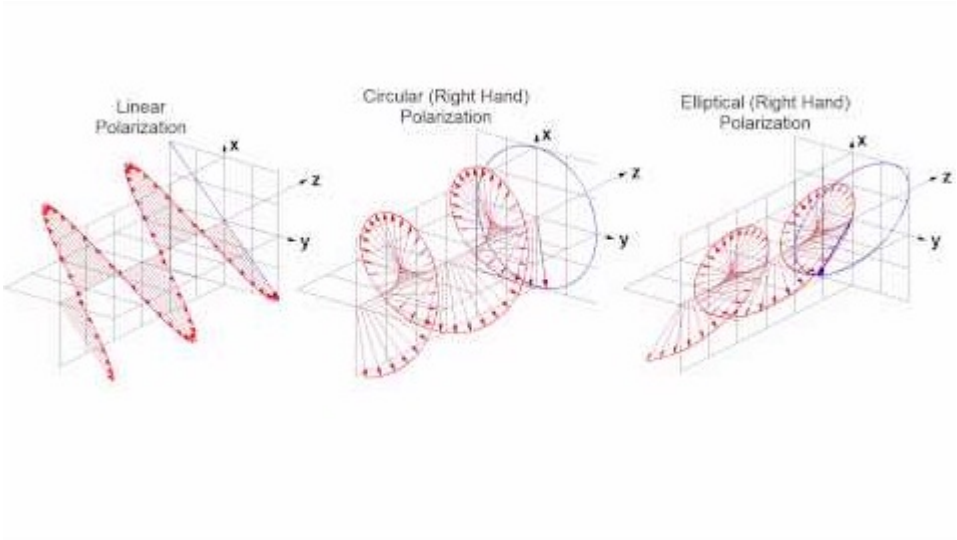

Figure 2.1: Linear, elliptical and circular polarizations[3]

$$\mathbf{B} = \mathbf{B_0} e^{\imath(\mathbf{k}.\mathbf{r}-\omega t)}; \tag{2.7}$$

where $\mathbf{k}$ is the wave-vector which specifies the direction of propagation, $\mathbf{r}$ is the position vector, t is time and ω is the angular frequency. In isotropic media, described by constant permittivity and permeability, vectors $\mathbf{E}, \mathbf{B}, \mathbf{k}$ form an orthogonal clockwise system. Because of this and Maxwell's equations, two of these vectors already allow us to compute the third. In our calculations, we'll use $\mathbf{k}$ to specify the wave's direction and $\mathbf{E}$ to specify its polarization - a general property of all vectorial waves describing the evolution of the vector in time and space .

Let us consider a plane wave with $\mathbf{k}$ pointing along the $\mathbf{z}$ direction. In this case, the electric field can only have $\mathbf{x}$ and $\mathbf{y}$ components(as shown in Fig.2.1) :

$$\mathbf{E}_x(z,t) = \hat{\mathbf{x}} E_{0x} e^{\imath(kz-\omega t)}, \tag{2.8}$$

$$\mathbf{E}_y(z,t) = \hat{\mathbf{y}} E_{0y} e^{\imath(kz-\omega t+\delta)}. \tag{2.9}$$

As a function of δ (here δ is the $phase\ difference$ between the y and x), we can have several kinds of polarizations: linear(for example$\delta = 0$), circular ($\delta = \frac{\pi}{2}$), elliptical ($\delta = \frac{\pi}{4}$) (See fig. 2.1) . Every polarization can by characterized by an angle of rotation (azimuth) and ellipticity (the major to minor axis ratio). Furthermore, we call a polarization transverse electric (TE) when there is no electric field in the direction of propagation (so it is parallel to the surface of the grating). In the opposite case, when the same can be said about the magnetic field, we call a polarization transverse magnetic (TM).

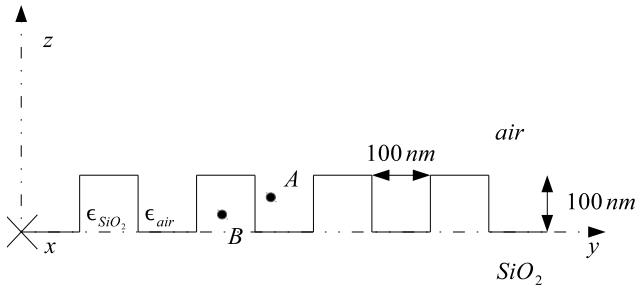

Figure 2.2: In our example, the permittivity tensor is diagonal in both materials (air and SiO_2), thus we can work with it as a scalar quantity. In points A and B, function $\epsilon(\mathbf{r})$ will have the following values : $\epsilon(\mathbf{A}) = \epsilon_{air}, \epsilon(\mathbf{B}) = \epsilon_{SiO_2}$. Furthermore, we can see that in the grating region,$\epsilon(\mathbf{r})$ is periodic in the y-direction with a period of 200nm, while constant in the direction of axes x and z, so $\Lambda_x = \Lambda_z = \infty$ and $\Lambda_y = 200nm$.

2.3 Periodic Media

A periodic medium for us is a medium in which permittivity is a periodic (repeating in space) function of the coordinates.

Let us assume an anisotropic medium described by a general relative permittivity tensor

$$\overleftrightarrow{\boldsymbol{\epsilon}}(\mathbf{r}) = \begin{pmatrix} \epsilon_{xx}(\mathbf{r}) & \epsilon_{xy}(\mathbf{r}) & \epsilon_{xz}(\mathbf{r}) \\ \epsilon_{yx}(\mathbf{r}) & \epsilon_{yy}(\mathbf{r}) & \epsilon_{yz}(\mathbf{r}) \\ \epsilon_{zx}(\mathbf{r}) & \epsilon_{zy}(\mathbf{r}) & \epsilon_{zz}(\mathbf{r}) \end{pmatrix}. \tag{2.10}$$

At optical frequencies, we can replace the permeability tensor with a scalar quantity:

$$\overleftrightarrow{\boldsymbol{\mu}} = \mu_0, . \tag{2.11}$$

In the general case, we can characterize the periodicity of the grating region with the so-called *grating vector* :

$$\mathbf{\Gamma} = \hat{\mathbf{x}}\Gamma_x + \hat{\mathbf{y}}\Gamma_y + \hat{\mathbf{z}}\Gamma_z, \tag{2.12}$$

where

$$|\mathbf{\Gamma}| = \Gamma = \frac{2\pi}{\Lambda} \tag{2.13}$$

and

$$\Gamma_i = \frac{2\pi}{\Lambda_i},\ i = x, y, z. \tag{2.14}$$

We have

$$\frac{1}{\Lambda^2} = \frac{1}{\Lambda_x^2} + \frac{1}{\Lambda_y^2} + \frac{1}{\Lambda_z^2}. \tag{2.15}$$

Here, $\hat{x}$, $\hat{y}, \hat{z}$ are unit vectors in the directions of the Cartesian axes, Λ is the grating period and Λ_x, Λ_y, $\Lambda_z$are the grating periods parallel to their respective axes.

Since $\overleftrightarrow{\boldsymbol{\epsilon}}(\mathbf{r})$is indeed periodic, it is favorable to expand the permittivity into a Fourier series:

$$\epsilon_{ij}(\mathbf{r}) = \sum_l \exp(\imath l \boldsymbol{\Gamma}.\mathbf{r})\epsilon_{ij,l}, \tag{2.16}$$

where i, j are coordinates and l specifies terms in the Fourier expansion.

We can rewrite equation (2.16) with normalized components:

$$\epsilon_{ij}(\overline{\mathbf{r}}) = \sum_l \exp(\imath l \mathbf{n}_\Gamma.\overline{\mathbf{r}})\epsilon_{ij,l}, \tag{2.17}$$

where (we use this to define p, q and s):

$$\mathbf{n}_\Gamma = \boldsymbol{\Gamma}\frac{c}{\omega} = \hat{\mathbf{x}}\frac{\lambda_0}{\Lambda_x} + \hat{\mathbf{y}}\frac{\boldsymbol{\lambda_0}}{\boldsymbol{\Lambda_y}} + \hat{\mathbf{z}}\frac{\lambda_0}{\Lambda_z} = p\hat{\mathbf{x}} + q\hat{\mathbf{y}} + s\hat{\mathbf{z}}, \tag{2.18}$$

and

$$\overline{\mathbf{r}} = \frac{\omega}{c}\mathbf{r}, \quad \overline{z} = \frac{\omega}{c}z, \quad \overline{y} = \frac{\omega}{c}y \quad \overline{x} = \frac{\omega}{c}x, \tag{2.19}$$

Now let's rewrite Maxwell's equations for the fields in equation (2.6) and equation (2.7):

$$\nabla \times \mathbf{E} = -\imath\omega\mathbf{B} = -\imath\omega\mu_{vac}\mathbf{H}, \tag{2.20}$$

$$\nabla \times \mathbf{B} = \imath\omega\mu_{vac}\epsilon_{vac}\boldsymbol{\epsilon}\mathbf{E}. \tag{2.21}$$

According to the Floquet theorem, the electric and magnetic fields of waves can be expressed as ,

$$\sqrt{\frac{\epsilon_{vac}}{\mu_{vac}}}\mathbf{E}(\overline{z}) = \sum_m \mathbf{e}_m(\overline{z})\exp(-\imath\mathbf{n}_m.\overline{\mathbf{r}}), \tag{2.22}$$

$$\sqrt{\frac{\mu_{vac}}{\epsilon_{vac}}}\mathbf{H}(\overline{z}) = \sum_m \mathbf{h}_m(\overline{z})\exp(-\imath\mathbf{n}_m.\overline{\mathbf{r}}); \tag{2.23}$$

where

$$\mathbf{e}_m(\bar{z}) = \hat{\mathbf{x}}\mathbf{e}_{xm}(\bar{z}) + \hat{\mathbf{y}}\mathbf{e}_{ym}(\bar{z}) + \hat{\mathbf{z}}\mathbf{e}_{zm}(\bar{z})_z, \tag{2.24}$$

$$\mathbf{h}_m(\bar{z}) = \hat{\mathbf{x}}\mathbf{h}_{xm}(\bar{z}) + \hat{\mathbf{y}}\mathbf{h}_{ym}(\bar{z}) + \hat{\mathbf{z}}\mathbf{h}_{zm}(\bar{z})_z, \tag{2.25}$$

and the normalized propagation vector of the m-th Fourier components has the form

$$\mathbf{n}_m(\bar{z}) = \hat{\mathbf{x}}p_m(\bar{z}) + \hat{\mathbf{y}}q_m(\bar{z}) + \hat{\mathbf{z}}s_m(\bar{z})_z. \tag{2.26}$$

Here,

$$p_m = mp, \quad q_m = mq + q_0, \quad s_m = ms, \tag{2.27}$$

with

$$q_0 = \sqrt{\epsilon^{(0)}}\sin(\varphi_i), \tag{2.28}$$

where φ_i is the angle of incidence.

2.4 Transfer Matrix

After some mathematical alterations detailed in [4], we get the following equations:

$$\frac{d}{d\bar{z}}\mathbf{f}_{\hat{t}} = \imath\mathbf{C}\mathbf{f}_{\hat{t}}, \tag{2.29}$$

$$\mathbf{f}_{\hat{n}} = \mathbf{D}\mathbf{f}_{\hat{t}}. \tag{2.30}$$

Here,

$$\mathbf{f}_{\hat{t}} = \begin{pmatrix} \mathbf{e}_x \\ \mathbf{h}_y \\ \mathbf{e}_y \\ \mathbf{h}_x \end{pmatrix}, \tag{2.31}$$

$$\mathbf{f}_{\hat{n}} = \begin{pmatrix} \mathbf{e}_z \\ \mathbf{h}_z \end{pmatrix}; \tag{2.32}$$

$$\mathbf{C} = \begin{pmatrix} \mathbf{p}\boldsymbol{\epsilon}_{zz}^{-1}\boldsymbol{\epsilon}_{zx} + \mathbf{s} & \mathbf{p}\boldsymbol{\epsilon}_{zz}^{-1}\mathbf{p} & \mathbf{p}\boldsymbol{\epsilon}_{zz}^{-1}\boldsymbol{\epsilon}_{zy} & -\mathbf{p}\boldsymbol{\epsilon}_{zz}^{-1}\mathbf{q} \\ \boldsymbol{\epsilon}_{xz}\boldsymbol{\epsilon}_{zz}^{-1}\boldsymbol{\epsilon}_{zx} - \boldsymbol{\epsilon}_{xx} + \mathbf{q}^2 & \boldsymbol{\epsilon}_{xz}\boldsymbol{\epsilon}_{zz}^{-1}\mathbf{p} + \mathbf{s} & \boldsymbol{\epsilon}_{xz}\boldsymbol{\epsilon}_{zz}^{-1}\boldsymbol{\epsilon}_{zy} - \boldsymbol{\epsilon}_{xy} + \mathbf{q}\mathbf{p} & -\boldsymbol{\epsilon}_{xz}\boldsymbol{\epsilon}_{zz}^{-1}\mathbf{q} \\ \mathbf{q}\boldsymbol{\epsilon}_{zz}^{-1}\boldsymbol{\epsilon}_{zx} & \mathbf{q}\boldsymbol{\epsilon}_{zz}^{-1}\mathbf{p} & \mathbf{q}\boldsymbol{\epsilon}_{zz}^{-1}\boldsymbol{\epsilon}_{zy} + \mathbf{s} & -\mathbf{q}\boldsymbol{\epsilon}_{zz}^{-1}\mathbf{q} + \mathbf{1} \\ \boldsymbol{\epsilon}_{yx} - \boldsymbol{\epsilon}_{yz}\boldsymbol{\epsilon}_{zz}^{-1}\boldsymbol{\epsilon}_{zx} + \mathbf{p}\mathbf{q} & -\boldsymbol{\epsilon}_{yz}\boldsymbol{\epsilon}_{zz}^{-1}\mathbf{p} & \boldsymbol{\epsilon}_{yy} - \boldsymbol{\epsilon}_{yz}\boldsymbol{\epsilon}_{zz}^{-1}\boldsymbol{\epsilon}_{zy} - \mathbf{p}^2 & \boldsymbol{\epsilon}_{yz}\boldsymbol{\epsilon}_{zz}^{-1}\mathbf{q} + \mathbf{s} \end{pmatrix}, \tag{2.33}$$

$$\mathbf{D} = \begin{pmatrix} -\boldsymbol{\epsilon}_{zz}^{-1}\boldsymbol{\epsilon}_{zx} & -\boldsymbol{\epsilon}_{zz}^{-1}\mathbf{p} & -\boldsymbol{\epsilon}_{zz}^{-1}\boldsymbol{\epsilon}_{zy} & \boldsymbol{\epsilon}_{zz}^{-1}\mathbf{q} \\ -\mathbf{q} & \mathbf{0} & \mathbf{p} & \mathbf{0} \end{pmatrix}, \tag{2.34}$$

where

$$\mathbf{p} = \begin{pmatrix} Mp & 0 & 0 & 0 & 0 \\ 0 & p(M-1) & 0 & 0 & 0 \\ 0 & 0 & ... & 0 & 0 \\ 0 & 0 & 0 & -p(M-1) & 0 \\ 0 & 0 & 0 & 0 & Mp \end{pmatrix}, \tag{2.35}$$

$$\mathbf{q} = \begin{pmatrix} q_0 + Mq & 0 & 0 & 0 & 0 \\ 0 & ... & 0 & 0 & 0 \\ 0 & 0 & q_0 & 0 & 0 \\ 0 & 0 & 0 & ... & 0 \\ 0 & 0 & 0 & 0 & q_0 - Mq \end{pmatrix}, \tag{2.36}$$

$$\mathbf{s} = \begin{pmatrix} Ms & 0 & 0 & 0 & ... \\ 0 & s(M-1) & 0 & ... & 0 \\ 0 & 0 & ... & 0 & 0 \\ 0 & ... & 0 & -s(M-1) & 0 \\ ... & 0 & 0 & 0 & -sM \end{pmatrix}, \tag{2.37}$$

$$\boldsymbol{\epsilon}_{ij} = \begin{pmatrix} \epsilon_{ij,0} & \epsilon_{ij,-1} & . & . & \epsilon_{ij,-M} \\ \epsilon_{ij,1} & \epsilon_{ij,0} & . & . & . \\ . & . & . & . & . \\ . & . & . & \epsilon_{ij,0} & \epsilon_{ij,-1} \\ \epsilon_{ij,M} & . & . & \epsilon_{ij,1} & \epsilon_{ij,0} \end{pmatrix}; \tag{2.38}$$

here M is the order of the Fourier expansion (can be any integer, it shows how precisely we approximate the periodic structure of permittivity).

The solution to eqs. 2.29, 2.30 reduces to a problem of finding the eigenvectors of matrix $\mathbf{C}$. Let $\kappa_r$denote an eigenvalue determined from the characteristic equation:

$$\det(\mathbf{C} - \kappa\mathbf{1}) = 0. \tag{2.39}$$

The corresponding (column) eigenvector will be denoted as $\boldsymbol{\nu}_r$(with elements $\boldsymbol{\nu}_{rl}$). Matrix $\mathbf{T}$ which is transforming $\mathbf{C}$ to a diagonal one is built of these eigenvectors, so

$$\mathbf{T} = \begin{pmatrix} \boldsymbol{\nu}_1 & \boldsymbol{\nu}_2 & ... & \boldsymbol{\nu}_n \end{pmatrix}. \tag{2.40}$$

We define vector $\mathbf{g}$, which multiplied by $\mathbf{T}$ gives $\mathbf{f}_{\hat{t}}$:

$$\mathbf{f}_{\hat{t}} = \mathbf{T}\mathbf{g}; \tag{2.41}$$

with further algebraic operations we get the following equations:

$$\frac{d}{d\bar{z}}\mathbf{T}^{-1}\mathbf{f}_{\hat{t}} = \imath\mathbf{T}^{-1}\mathbf{C}\mathbf{T}\mathbf{T}^{-1}\mathbf{f}_{\hat{t}}, \tag{2.42}$$

$$\frac{d}{d\bar{z}}\mathbf{g} = \imath\boldsymbol{\kappa}\mathbf{g}, \tag{2.43}$$

where $\boldsymbol{\kappa} = \delta_{rl}\kappa_l$is a diagonal matrix and $\mathbf{g}$ is a column vector.

For homogenous and isotropic regions, we get:

$$\mathbf{T} = \begin{pmatrix} \dot{\mathbf{q}} & \dot{\mathbf{p}} & \dot{\mathbf{q}} & \dot{\mathbf{p}} \\ \dot{\mathbf{q}}\xi & \epsilon\dot{\mathbf{p}}\xi^{-1} & -\dot{\mathbf{q}}\xi & -\epsilon\dot{\mathbf{p}}\xi^{-1} \\ -\dot{\mathbf{p}} & \dot{\mathbf{q}} & -\dot{\mathbf{p}} & \dot{\mathbf{q}} \\ \dot{\mathbf{p}}\xi & -\epsilon\dot{\mathbf{q}}\xi^{-1} & -\dot{\mathbf{p}}\xi & \epsilon\dot{\mathbf{q}}\xi^{-1} \end{pmatrix}, \tag{2.44}$$

where

$$\dot{\mathbf{p}} = \delta_{nl}\dot{p}_l \tag{2.45}$$

$$\dot{\mathbf{q}} = \delta_{nl}\dot{q}_l \tag{2.46}$$

$$\dot{\boldsymbol{\xi}} = \delta_{nl}\xi_l, \tag{2.47}$$

$$\xi_m = (\epsilon - n_{\hat{t}m})^{1/2}, \tag{2.48}$$

$$n_{\hat{t}m} = (p_m^2 + q_m^2)^{1/2}, \tag{2.49}$$

$$\dot{p}_m = \frac{p_m}{n_{\hat{t}m}}, \tag{2.50}$$

$$\dot{q}_m = \frac{q_m}{n_{\hat{t}m}}. \tag{2.51}$$

The corresponding column vector becomes :

$$\mathbf{g} = \begin{pmatrix} \mathbf{g}^+ \\ \mathbf{g}^- \end{pmatrix} = \begin{pmatrix} {}^{TE}\mathbf{g}^+ \\ {}^{TM}\mathbf{g}^+ \\ {}^{TE}\mathbf{g}^- \\ {}^{TM}\mathbf{g}^- \end{pmatrix}, \tag{2.52}$$

where elements of the column vectors can be written as :

$${}^{TE}\mathbf{g}^{\pm} = \begin{pmatrix} {}^{TE}g_M^{\pm} \\ \cdot \\ \cdot \\ {}^{TE}g_0^{\pm} \\ \cdot \\ \cdot \\ {}^{TE}g_{-M}^{\pm} \end{pmatrix}, \tag{2.53}$$

$${}^{TM}\mathbf{g}^{\pm} = \begin{pmatrix} {}^{TM}g_M^{\pm} \\ \cdot \\ \cdot \\ {}^{TM}g_0^{\pm} \\ \cdot \\ \cdot \\ {}^{TM}g_{-M}^{\pm} \end{pmatrix}, \tag{2.54}$$

For example, ${}^{TM}g_3^{(0)-}$ indicates the third diffraction order (3 in the subscript) of the incident(signed by the $-$) TM wave in the region above the grating ((0) in the superscript) (as shown in fig.2.3).

Ultimately, all the information about the grating can be expressed using the transfer matrix (superscripts indicate the region or boundary which the matrices characterize)

$$\mathbf{W} = \mathbf{B}^{(01)}\mathbf{U}^{(1)}(\bar{d}_1)\mathbf{B}^{(12)}. \tag{2.55}$$

Here

$$\mathbf{U}^{(1)}(\bar{d}_1) = \exp(\imath\boldsymbol{\kappa}^{(1)}\bar{d}_1), \tag{2.56}$$

$$\mathbf{B}^{(01)} = \left[\mathbf{T}^{(0)}\right]^{-1}\mathbf{T}^{(1)}, \tag{2.57}$$

$$\mathbf{B}^{(12)} = \left[\mathbf{T}^{(1)}\right]^{-1}\exp(-\imath\mathbf{s}^{(1)}\bar{d}_1)\mathbf{T}^{(2)}. \tag{2.58}$$

Here $\bar{d}_1 = \frac{\omega}{c}d_1$is the normalized thickness of the grating.

Matrix $\mathbf{W}$ relates vectors $\mathbf{g}^{(0)}$and $\mathbf{g}^{(2)}$ the following way:

$$\mathbf{g}^{(0)} = \begin{pmatrix} \mathbf{g}^{(0)+} \\ \mathbf{g}^{(0)-} \end{pmatrix} = \begin{pmatrix} \mathbf{W}_1 & \mathbf{W}_2 \\ \mathbf{W}_3 & \mathbf{W}_4 \end{pmatrix} \begin{pmatrix} \mathbf{g}^{(2)+} \\ \mathbf{g}^{(2)-} \end{pmatrix} = \mathbf{W}\mathbf{g}^{(2)}. \tag{2.59}$$

The wave of unit amplitude incident from region (0) onto the grating with TE/TM polarization is defined by :

$${}^{TE}\mathbf{g}^{(0)-} = \begin{pmatrix} 0 \\ . \\ 0 \\ 1 \\ 0 \\ . \\ 0 \end{pmatrix}, \quad {}^{TM}\mathbf{g}^{(0)-} = 0, \tag{2.60}$$

$${}^{TM}\mathbf{g}^{(0)-} = \begin{pmatrix} 0 \\ . \\ 0 \\ 1 \\ 0 \\ . \\ 0 \end{pmatrix}, \quad {}^{TE}\mathbf{g}^{(0)-} = 0. \tag{2.61}$$

We shall assume that there is no wave propagating from region(0) towards the grating region (1) . The incident wave generates reflected ($\mathbf{g}^{(0)+}$) and transmitted ($\mathbf{g}^{(2)-}$) waves.

Assuming the situation described above and using equation 2.59, we get :

$$\mathbf{g}^{(2)-} = (\mathbf{W}_4)^{-1}\mathbf{g}^{(0)-}, \tag{2.62}$$

$$\mathbf{g}^{(0)+} = \mathbf{W}_2(\mathbf{W}_4)^{-1}\mathbf{g}^{(0)-}. \tag{2.63}$$

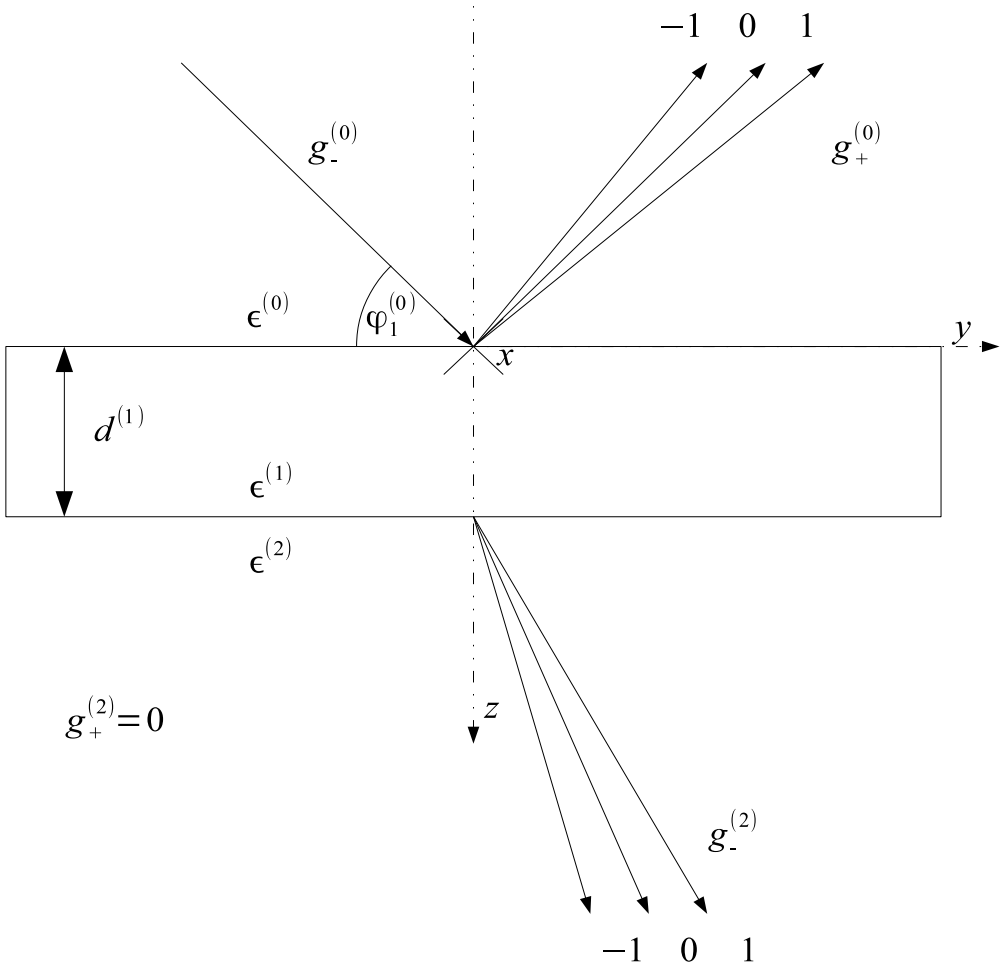

Figure 2.3: The geometric situation

The power carried by a wave of the m-th diffraction order propagating with the normal, *i.e.*, the $\bar{z}$ component of the normalized propagation vector oriented parallel or anti-parallel with respect to $\hat{\mathbf{z}}$ in region I $(I = 0, 2)$ with TE and TM polarizations is given by:

$$^{TE}p_m^{(I)\pm} = \Re(\xi_m)|^{TE}g_m^{(I)\pm}|^2, \tag{2.64}$$

$$^{TM}p_m^{(I)\pm} = \Re(\frac{\epsilon^{(I)}}{\xi_m})|^{TM}g_m^{(I)\pm}|^2. \tag{2.65}$$

Chapter 3

Numerical Simulations

With the aim of numerically solving the aforementioned problem, specifically, to compute $\mathbf{g}^{(2)-}$ and $\mathbf{g}^{(0)+}$, a program was written in the programming language Mathematica.

3.1 Wolfram Mathematica

Mathematica [5] is a computational software program used in scientific, engineering, and mathematical fields and other areas of technical computing. It was conceived by Stephen Wolfram and is developed by Wolfram Research of Champaign, Illinois . One of its strengths is the potential of symbolic calculations, which for say a problem with a symmetry can dramatically reduce calculation times. It was chosen because of the ease it handles matrix operations with (the creation of matrix $\mathbf{C}$ from its submatrices, then the division of matrix $\mathbf{W}$ to submatrices). The numerically most challenging part (computing the eigenvalues and eigenvectors of $\mathbf{C}$ for matrices $\mathbf{T}$and $\boldsymbol{\kappa}$) could also be done without problems.

3.2 The Code

As an input, we always had the permittivities of the materials used in the grating as a function of the energy of the light, and of course the geometric structure of the grating. From here, our aim was to calculate $\mathbf{g}^{(0)+}$, specifically, to compute the Kerr rotation of the reflected light then to compare it to the experimental results (for more details, see chapter 4). In our case, the surface of the grating was rectangular, so we used a combination of Heaviside functions to model it (see algorithm 3.1) (the Heaviside theta function is a function which is 0 for negative values and 1 positive values and zero):

From this, we then substitute to the equations outlined, and arrive to the vector $\mathbf{g}^{(0)+}$, which contains all the information we need, specifically, the Kerr rotation and ellipticity to compare with experimental measurements:

$$ {}^{TE}\Theta_j = {}^{TE}\theta_j + \imath\, {}^{TE}\epsilon_j = \frac{{}^{TM}g_j^{\pm}}{{}^{TE}g_j^{\pm}}, \tag{3.1} $$

where ${}^{TE}\theta_j$ is the rotation of polarization in the j-th diffraction order for incoming TE waves

Algorithm 3.1 Calculating the Fourier coefficients for the surface permittivity. Here, g is the order of expansion, x is the function variable and $\frac{ii}{\pi}$ is the ratio of the length of protruding part to the whole period (We're working with a one-dimensionally periodic region. Furthermore, ExxFourier is a vector of ϵ_{xx}'s Fourier expansion; we can see that in between the protruding parts it is supposed to be 1 (we're working with relative permittivities). Similarly, ϵ_{xy} is supposed to be zero in between the protruding parts, because the permittivity of air is diagonal).

```
FC = Table[ FourierCoefficient[(HeavisideTheta[x + ii*(Pi*1)/1090.] - HeavisideTheta[x - ii*(Pi*1)/1090.]), x, k], {k, -(g - 1), (g - 1)}];
Unitvector = Table[KroneckerDelta[i, g], {i, 2 g - 1}];
ExxFourier = Table[FC*(Permit[[i, 2]] - 1) + Unitvector, {i, n}];
ExyFourier = Table[FC*(Permit[[i, 3]] ), {i, n}];
```

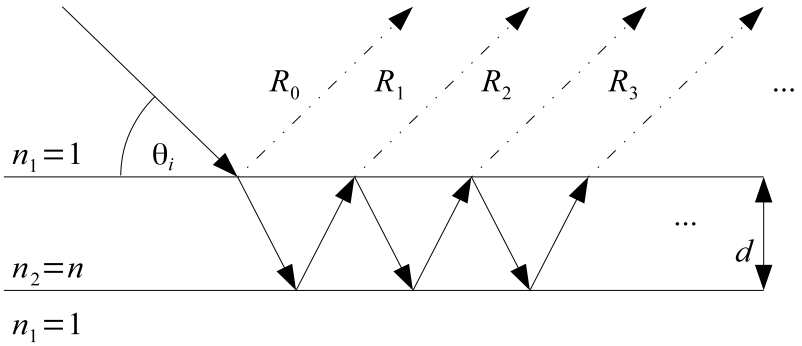

Figure 3.1: Fabry-Pérot etalon

and ${}^{TE}\epsilon_j++$ is the j-th order ellipticity . Similarly for TM waves :

$$ {}^{TM}\Theta_j = {}^{TM}\theta_j + \imath {}^{TM}\epsilon_j = \frac{{}^{TE}g_j^{\pm}}{{}^{TM}g_j^{\pm}}. \tag{3.2} $$

3.3 Fabry–Pérot etalon

A Fabry-Pérot etalon is made of a transparent plate with two reflective surfaces (as shown in figure 3.1)

As follows from Fresnell's equations, reflectivities for the s and p polarizations are[6] :

$$ R_s = \left(\frac{n_1 \cos(\theta_i) - n_2 \sqrt{1 - \left(\frac{n_1}{n_2}\sin(\theta_i)\right)^2}}{n_1 \cos(\theta_i) + n_2 \sqrt{1 - \left(\frac{n_1}{n_2}\sin(\theta_i)\right)^2}} \right)^2, \tag{3.3} $$

$$R_p = \left(\frac{-n_2 \cos(\theta_i) + n_1 \sqrt{1 - \left(\frac{n_1}{n_2} \sin(\theta_i)\right)^2}}{n_2 \cos(\theta_i) + n_1 \sqrt{1 - \left(\frac{n_1}{n_2} \sin(\theta_i)\right)^2}} \right)^2 . \tag{3.4}$$

Furthermore, if we calculate the interference of infinity reflections (like in figure 3.1), then we get as the final result the reflective function:

$$R_e = \frac{I_r}{I_i} = \frac{F \sin^2(\frac{\delta}{2})}{1 + F \sin^2(\frac{\delta}{2})}, \tag{3.5}$$

where

$$F = \left(\frac{2R}{1 - R^2} \right)^2 \tag{3.6}$$

is the coefficient of finesse and

$$\delta = \left(\frac{2\pi}{\lambda} \right) 2 n_2 d \cos(\theta_t) \tag{3.7}$$

is the phase difference between each succeeding reflection (θ_t is the angle of light inside the material).

Now we attempt to calculate R_e using our numerical model and compare the results. To model the situation, we are using a thin plate made of $SiO_2$with a varying thicknesses and angle of incidences. The (diagonal) permittivity is dependent on the wavelength. Also, because this is not a periodic medium, we have $\Lambda_x = \Lambda_y = \Lambda_z = 0$. The results obtained by the analytical formulae along with the numerical model are shown in figures 3.2, 3.3, 3.4.

From the above results it follows that the results obtained for the special case are in accordance with our methods of computation.

3.4 Possible applications in solar cell technology

Light trapping is one of the major topics in solar cell research. Basically, it deals with preventing light that has entered the solar cell from leaving it again and thus increasing the probability of it being absorbed. One way to achieve this is to increase the internal path length of light inside a solar cell by diffraction with optical nanostructures [7]. The basic idea of using a grating is that incident light is diffracted into several paths. An optimized grating will diffract as much light as possible into directions close to parallel to the surface - thus, it will travel a long distance through the solar cell before escaping.

The photocurrent density produced by the solar cell is given by [7]:

$$j_{ph} = -e_0 \int_{\lambda_1}^{\lambda_2} \Phi_{AM1.5}(\lambda) abs(\lambda) d\lambda. \tag{3.8}$$

Here, e_0 is the elementary charge, $abs(\lambda)$ is the spectrally dependent absorption coefficient of the solar cell, and $\Phi_{AM1.5}$ is the photon flux in the AM1.5 G spectrum.

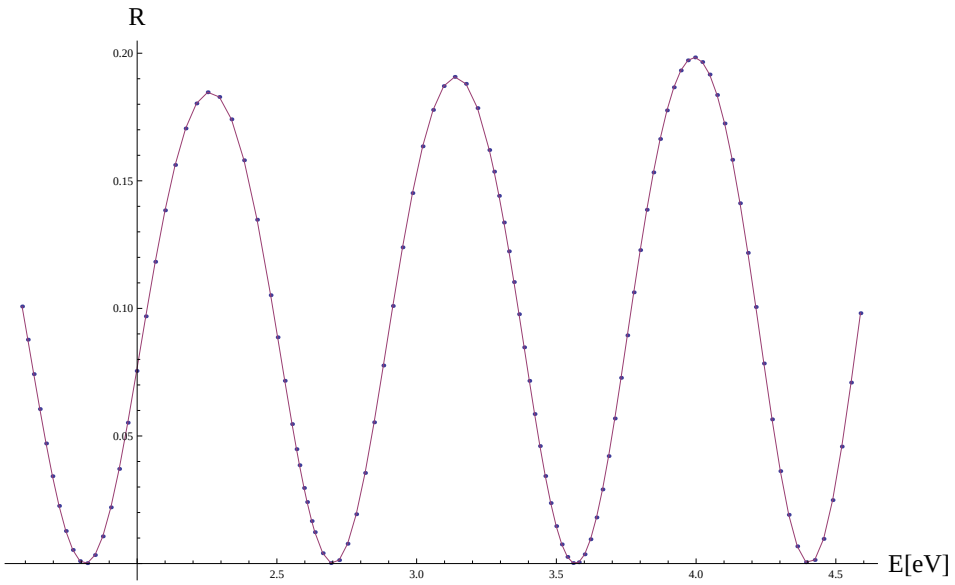

Figure 3.2: Reflection coefficient as a function of the light-wave's energy. The continuous line represents the results obtained with the methods above and the dots those obtained with our theoretical model. The angle of incidence is 30 degrees and the etalon is 500 nm thick.

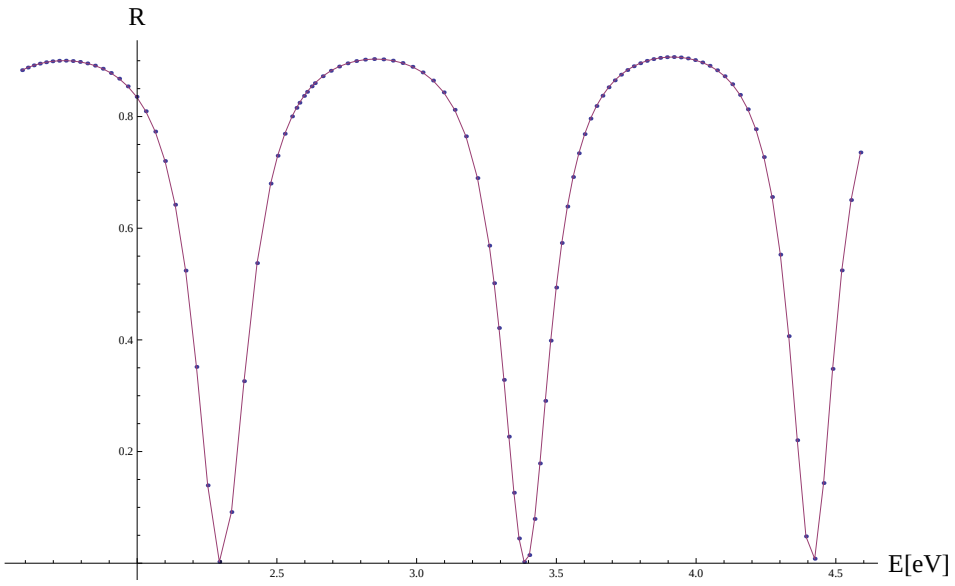

Figure 3.3: Reflection coefficient as a function of the light-wave's energy. The continuous line represents the results obtained with the methods above and the dots those obtained with our theoretical model. The angle of incidence is 80 degrees and the etalon is 500 nm thick.

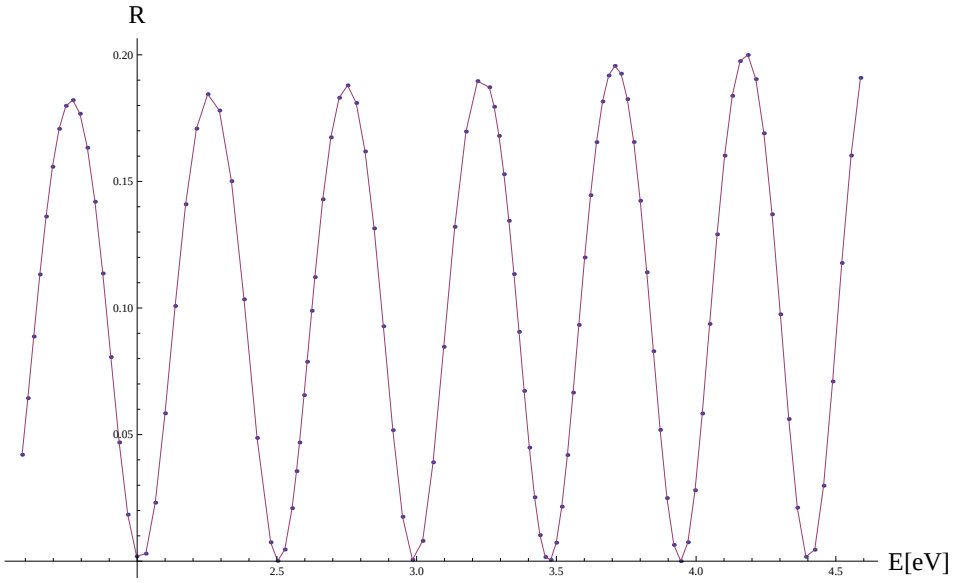

Figure 3.4: Reflection coefficient as a function of the light-wave's energy. The continuous line represents the results obtained with the methods above and the dots those obtained with our theoretical model. The angle of incidence is 30 degrees and the etalon is 900 nm thick.

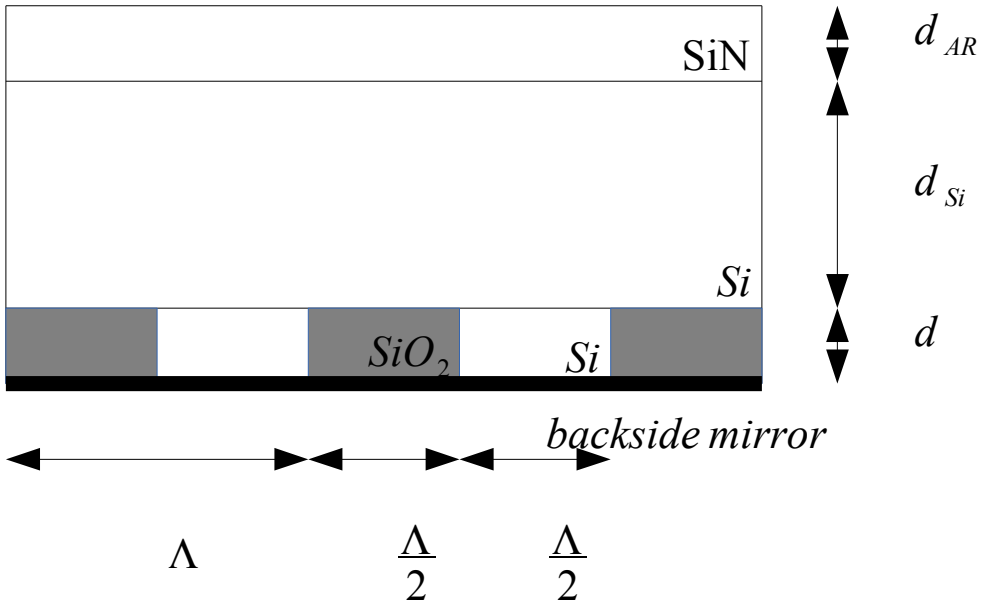

Figure 3.5: The inspected model of a solar cell

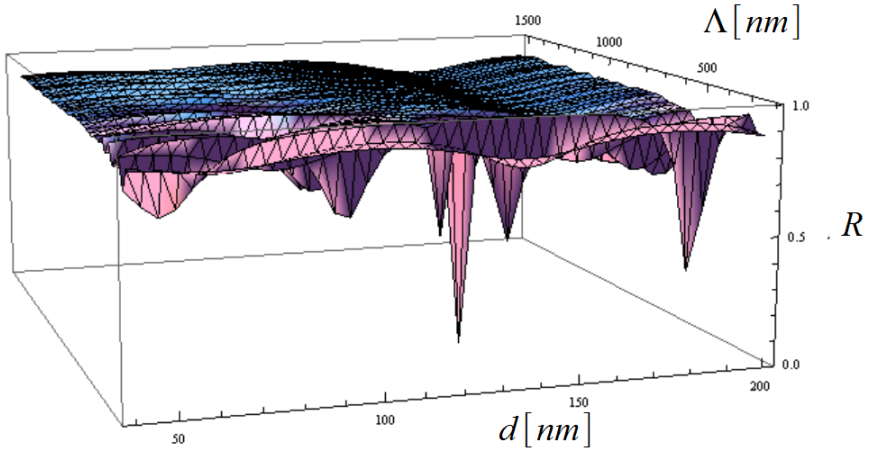

Figure 3.6: Reflection coefficient as a function of Λ and d. It can be seen that R has several local minima; in a setting without a grating or without properly chosen parameters the refraction efficiency is around 0.9.

In our example, we consider a structure consisting of a SiN antireflection coating with a thickness of $d_{AR} = 67.8nm$, a layer of crystalline silicon with a thickness of $d_{Si} = 40\mu m$, a diffraction grating consisting of Si and SiO_2 with its period (Λ) and thickness (d) as variables, and finally a backside mirror (as shown in figure 3.5). This case was inspected for a single wavelength of light ($1.36\mu m$) for the sake of simplicity.

Since the photocurrent is proportional to the absorbed light's energy, the lesser the reflected light's energy the more energy is absorbed inside the medium. Because reflectivity is easy to calculate from our model, we used it to judge the effectiveness of various configurations. In figure 3.6 we can see the reflection coefficient as a function of d and Λ. For $d = 125nm$ and $\Lambda = 400nm$ we get the lowest value of reflection in the inspected interval; we can see that with these parameters, more energy is absorbed inside the solar cell, thus its efficiency is higher.

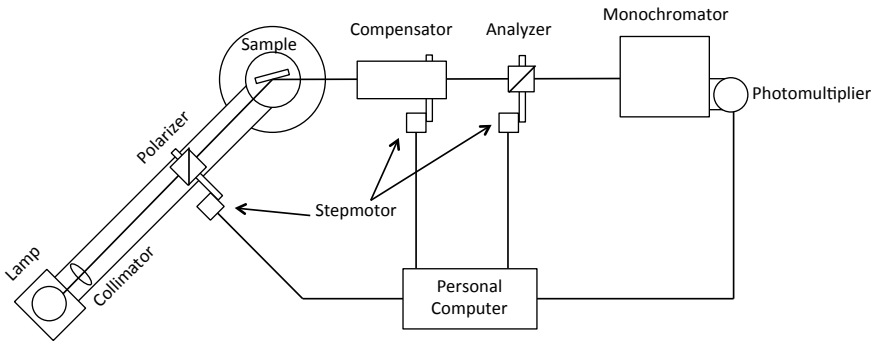

Figure 4.1: Experimental setup of four zone null ellipsometer for scatterometric experiments.

Chapter 4

Experimental Results

4.1 Ellipsometer

In our experiments, we used a four-zone null ellipsometer.

Spectroscopic ellipsometry is an experimental technique that measures the change of incident light polarization upon its reflection (or sometimes transmission). The exact nature of polarization change is determined by the material and geometry of the nanostructured array. If the material of the sample is isotropic, then the Jones reflection matrix is diagonal and there is no interaction between the s and p waves. The diagonal elements are related to the array structure and its optical properties. The ellipsometric angles Ψ and Δ are then defined by following equation:

$$\varrho = \frac{r_{pp}}{r_{ss}} = \tan\Psi e^{\imath\Delta}. \tag{4.1}$$

Spectral dependence of Ψ and Δ obtained by SE carries the important information about the geometry of nanostructured arrays.Typical ellipsometric experimental setup is the high power arc lamp–polarizer–sample–compensator–analyzer. This so-called PSCA optical sequence is widely used in standard ellipsometric setups. Detailed information about the main ideas of ellipsometry including basic notions on polarization and experimental techniques is treated in the book written by Azzam and Bashara [8].

Here, we restrict ourselves to the description of a specific four zone ellipsometric configuration

which was used in our experiments. This experiential setup is depicted in Fig. 4.1. An optical sequence of this null ellipsometer is polarizer–sample–compensator–analyzer (PSCA), where the compensator is a phase-retarding tool. The Jones vector of the light at the output of the analyzer (and the intensity detected by the detector as well) depends on the rotation angles of polarizer, compensator and analyzer α, β, γ. By searching the right values of α and β at a fixed γ the null ellipsometry provides a zero intensity of the light at the output.

4.2 Magneto-optical spectrometer based on the azimuth modulation technique

A magneto-optical spectrometer was also used to obtain data - the experimental setup for the measurement of the Kerr rotation was developed by Kahn and later extended for the extraction of Kerr ellipticity.

When an external magnetic field is applied to a ferromagnetic sample, it induces magneto-optical anisotropy. The off-diagonal elements of the Jones reflection matrix become in general nonzero, which indicates the conversion between s incident and p reflected (r_{ps}) as well as p incident and s reflected (r_{sp}) waves. Although the Jones reflection matrix has generally four elements, it can be simplified if the magnetic field is applied in the certain directions (e.g. perpendicular to the sample) [4].

There are two basic classes of experimental techniques which are employed for studies of weak MO effects. The first class is measuring the direct change of the intensity of light at the output of an optical element sequence. The second class, more sophisticated one, is based on the modulation of azimuth or ellipticity of incident light. In combination with a synchronic detection system, modulation techniques increase the signal-to-noise ratio. However, both classes are used in different specific situations (Kerr microscopy, Kerr vector magnetometry, Kerr spectroscopy, etc.).

There are two basic techniques using the time modulation of the light polarization. First, an intensity-based method is based on the modulation of ellipticity of a light wave using the photoelastic modulator. This method allows fast measurement, which makes it suitable for studying dynamics of magnetization processes. Because it is an intensity method, the calibration of the equipment is required in each measurement, which makes it inconvenient for spectroscopic experiments. The second experimental technique employs the Faraday rotation in glass for the modulation of the azimuth of the polarization ellipse. Such a modulator, called the Faraday cell, consists of a fused quartz rod with optically polished faces, inserted into a solenoid coil. Owing to the sinusoidal time dependence of the modulation current in the coil generated by a high power audio amplifier, the azimuth of the light wave passing through the cell is harmonically modulated in time. One can imagine the Faraday cell as a rotator with time dependent angle of rotation. A typical sequence of optical elements in a null MO spectrometer based on the azimuth modulation technique (depicted in Fig. 4.2) is high power arc lamp–monochromator–polarizer compensating Faraday rotator modulating Faraday rotator–phase plate (for Kerr ellipticity measurements)–sample–analyzer–photomultiplier. In the small angle approximation, the complex MOKE is measured as the ratio

$$\frac{r_{sp}}{r_{ss}} \approx \theta_K + i\epsilon_K$$

or

$$-\frac{r_{ps}}{r_{pp}} \approx \theta_K + i\epsilon_K,$$

where the indecent light beam is s- or p-polarized, respectively. Here θ_K and ϵ_K denote the Kerr rotation and ellipticity. Compensating Faraday cell automatically turns the plane of polarization by a certain angle to adjust detected intensity approximately to zero. Therefore it compensates all changes produced by MO effects in the sample or by rotation of the polarizer. This Faraday cell is controlled by negative feedback loop. Measured signal on the output is then proportional to the magneto-optical effect of the sample and it decreases with increasing amplification of the feedback regulator. The negative feedback is introduced by means of analog output signal from the lock-in detector. This signal is used to control the current supply for the compensating cell.

Such compensation technique with azimuth modulation has several advantages over the other experimental methods. Azimuth modulation with synchronic detection notably increases the signal to noise ratio. The intensity dependence at the output is a linear function of the deviation from crossed polarizers. Crossing of the polarizers can be completely automatic (controlled by the negative feedback loop) and very precise without mechanical input. The value of the measured angle is not dependent on the intensity of output light (null method). Therefore if a highly stable current supply for the compensating Faraday cell is used, very small MOKE angles down to the order of one millidegree can be measured. On the other hand the usage of Faraday cells limits the photon energy range of the measured spectrum. Typically the energy range is from 1.2 to 6 eV [9].

There were three types of experiments conducted: magneto-optic with perpendicular incidence and polar magnetization, another magneto-optic with a non-perpendicular incidence in longitudinal magnetization and ellipsometric experiments without any magnetization.

4.3 The Sample

The investigated sample consisted of a layer of rectangular permalloy grating on a layer of silicon (with a thickness that for our purposes can be considered infinite) , as pictured in figure 4.3. In the theoretical model we described it as a layer of alternating oxygen and permalloy, a layer of permalloy and a half-space of silicon. Aside from the factory data (a period of $1000nm$, a top line width of $400nm$, a $32nm$ thick $NiFe$ layer and the relief $16nm$ deep), AFM experiments have also been conducted, yielding the following results:

period -$1091.5nm$, top line width - $359.4nm$, depth of the relief - $21.7nm$; AFM cannot measure the thickness of the $NiFe$ layer, so we used the factory value - $32nm$ (see fig. 4.4 for more details).

4.4 Longitudinal magnetization

In a longitudinal magnetic field (the magnetic field is parallel to the surface of the grating), the permittivity tensor has the following form:

$$\overleftrightarrow{\boldsymbol{\epsilon}} = \begin{pmatrix} \epsilon_1 & 0 & \imath\epsilon_2 \\ 0 & \epsilon_1 & 0 \\ -\imath\epsilon_2 & 0 & \epsilon_1 \end{pmatrix}. \tag{4.2}$$

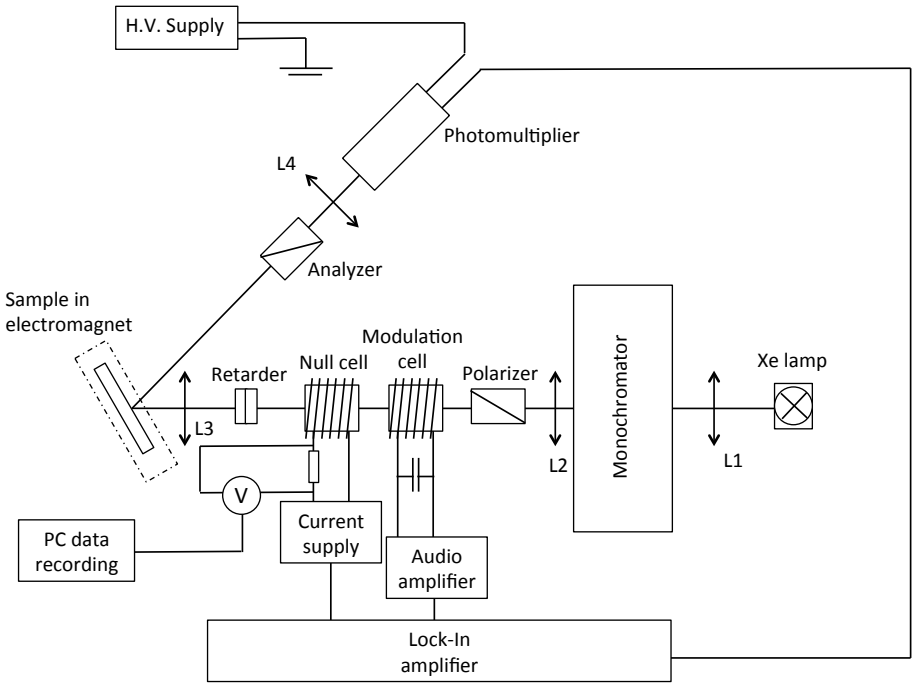

Figure 4.2: As a light source, a high pressure $450W$ Xe lamp was used. Afterward, the light was monochromatized by a prism monochromator. All optical elements, including lenses and glass rods for modulation and the null cell, were made of suprasil quartz glass with extended transmission to UV. The temperature of the Faraday cells was kept constant using a closed water circuit with a termostat. The signal modulation frequency was approximately $2kHz$. A pair of calcite polarizers served as the polarizer and analyzer. To detect the signal in the blue region and near UV, a photomultiplier tube was employed. The synchronic detection was provided by a lock-in amlifier. The negative feedback is introduced by means of analog output signal from the lock-in detector. This signal feedback is introduced by means of analog output signal from the lock-in detector. This signal is used to control the current supply for the null cell. Owing to the very high stability of this supply, the resolution of the spectrometer is the order of $10^{-4}deg$.The measured sample is mounted in an electromagnet with a variable magnetic circuit to measure the Kerr effect in polar, longitudinal or transverse geometry. During the measurement, usual values of the magnetic field were $470mT$ at $2A$ for the polar configuration and $100mT$ at $2A$ for the longitudinal configuration.

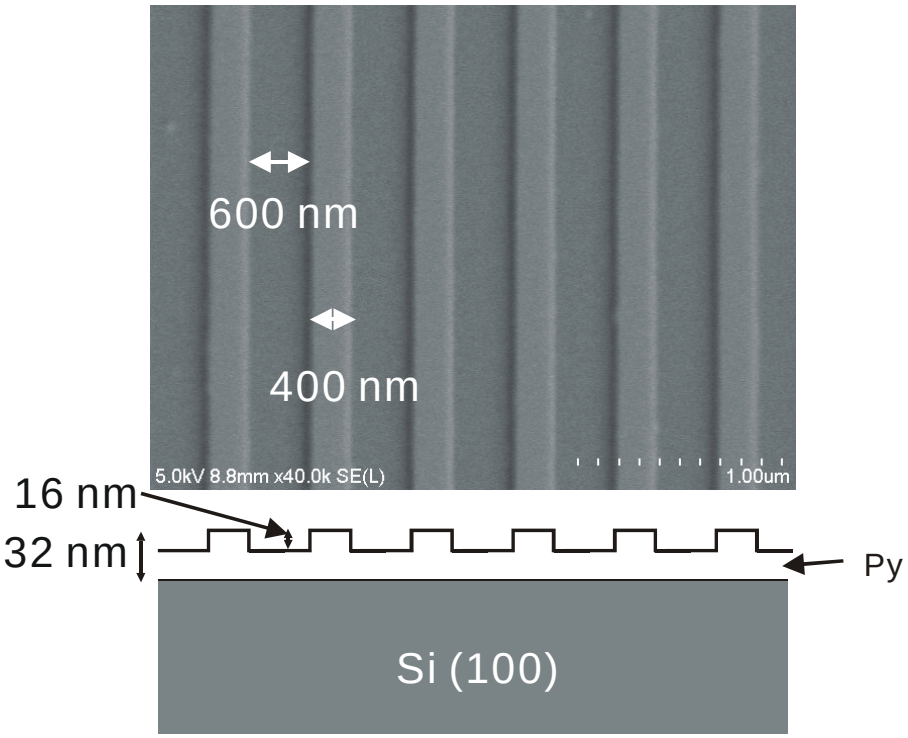

Figure 4.3: The factory data

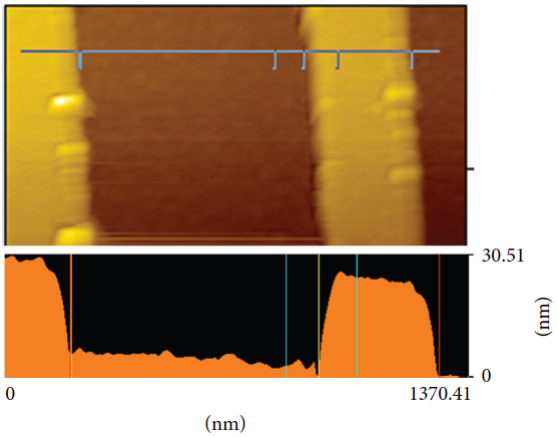

Figure 4.4: AFM measurements

The angle of incidence was 56 degrees in this case. In these graphs we also included an illustration of changing the order of the Fourier series, and the effect it has on the results (see figures 4.5, 4.6). From the results we can see that the data from the AFM experiments approximate the grating more accurately. Besides these graphs, all the other calculations use a fixed 10th order Fourier series. The higher the order of approximation, the more accurate is the approximation of the rectangular grating; however, increasing it also increases computation time as the matrices increase in size with the order linearly.

4.5 Polar magnetization

In a polar magnetic field (the magnetic field is perpendicular to the surface of the grating), the permittivity tensor has the following form:

$$\overleftrightarrow{\boldsymbol{\epsilon}} = \begin{pmatrix} \epsilon_1 & \imath\epsilon_2 & 0 \\ -\imath\epsilon_2 & \epsilon_1 & 0 \\ 0 & 0 & \epsilon_1 \end{pmatrix}. \tag{4.3}$$

The angle of incidence was approximately 0 degrees in this case. Aside from the experimental data and the standard calculations, we also include approximate calculations based on the so-called local method, which deals with only planar surfaces; we get the final result from a linear combination of a grating with Ni layers with thicknesses $16nm$ (or$10nm$ in the other case) and a $32nm$ respectively (as shown in fig.4.7, 4.8). For more details on the model, see [10].

From the results we can see that the data from the AFM experiments approximate the grating more accurately. The local method fails in this case; it only gives a rough approximation.

4.6 Ellipsometric experiments

In an ellipsometric setting, the permittivity tensor is diagonal:

$$\overleftrightarrow{\boldsymbol{\epsilon}} = \begin{pmatrix} \epsilon_1 & 0 & 0 \\ 0 & \epsilon_1 & 0 \\ 0 & 0 & \epsilon_1 \end{pmatrix}. \tag{4.4}$$

The angle of incidence was 60 degrees. In figures 4.9 and 4.10 the real and imaginary parts of ρ described in equation 4.1 are shown.

It can be seen that calculations from AFM measurements' parameters yield results that are in general closer to the experimental data.

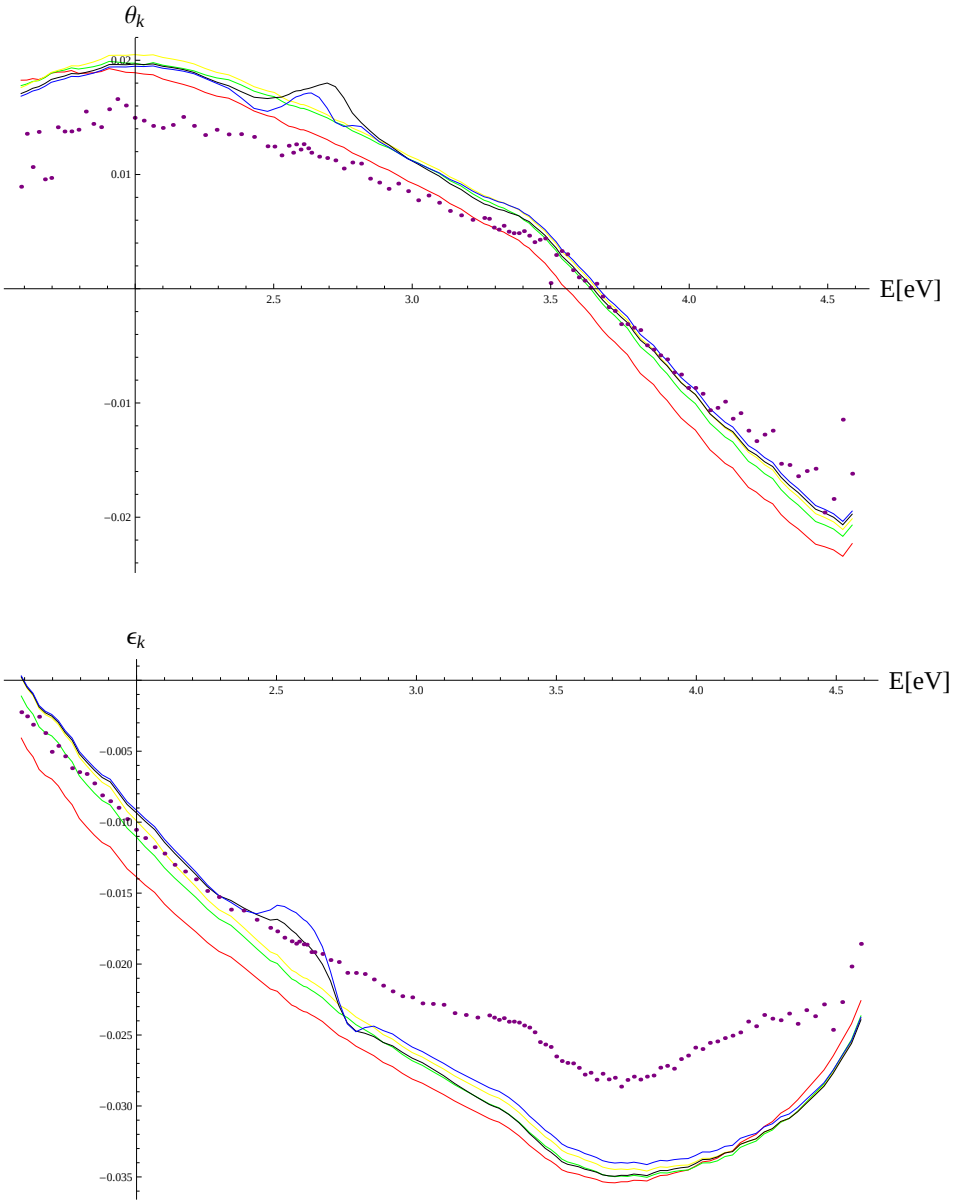

Figure 4.5: Kerr rotation (θ_k) and ellipticity (ϵ_k) as a function of light energy for the factory data. Dots represent the experimental results while the continuous lines represent the theoretical predictions with the order of the Fourier series (1 means that we used the -1st, 0th and 1st coefficients) as it follows: red - 1, green - 3, yellow - 7, black - 15, blue - 22. Some of the higher order calculations show fluctuations which are possibly caused by numerical instabilites

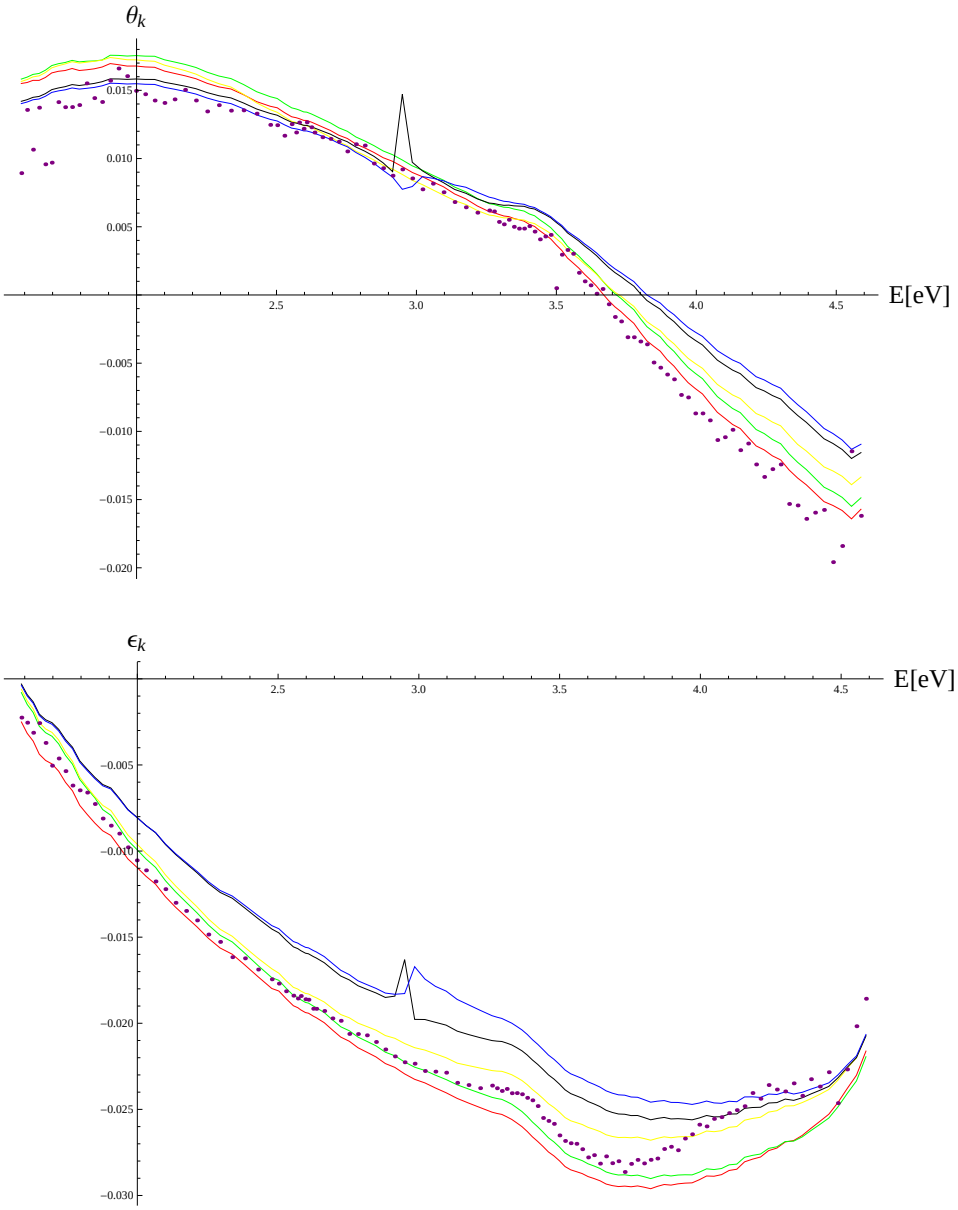

Figure 4.6: Kerr rotation (θ_k) and ellipticity (ϵ_k) as a function of light energy for the data from the AFM measurements. Dots represent the experimental results while the continuous lines represent the theoretical predictions with the order of the Fourier series (1 means that we used the -1st, 0th and 1st coefficients) as it follows: red - 1, green - 3, yellow - 7, black - 15, blue - 22. Some of the higher order calculations show fluctuations which are possibly caused by numerical instabilites.

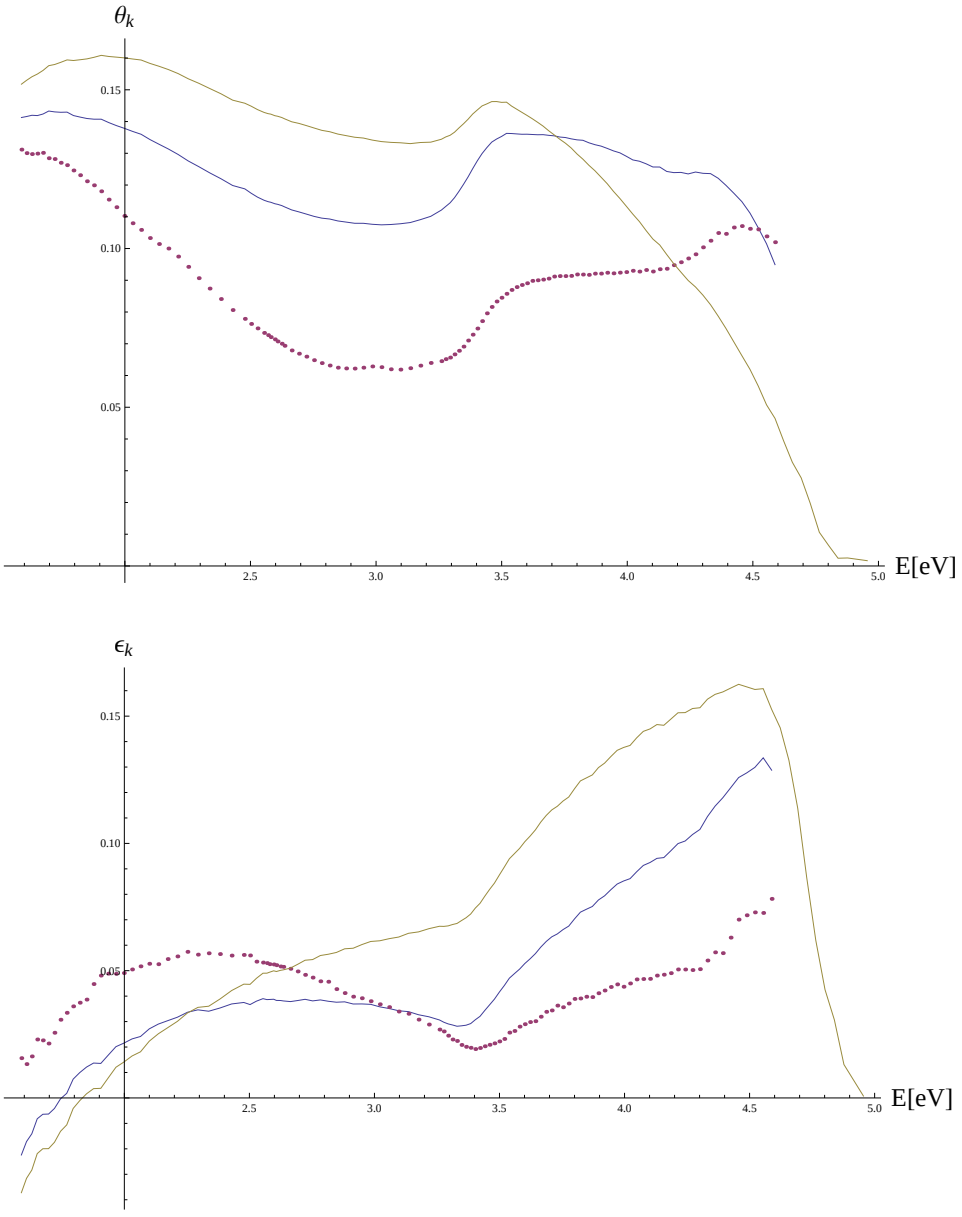

Figure 4.7: Kerr rotation (θ_k) and ellipticity (ϵ_k) as a function of light energy for the factory data. Dots represent the experimental results while the continuous lines represent the theoretical predictions; blue represents the results from the standard model while khaki represents the simpler model with the planar surfaces.

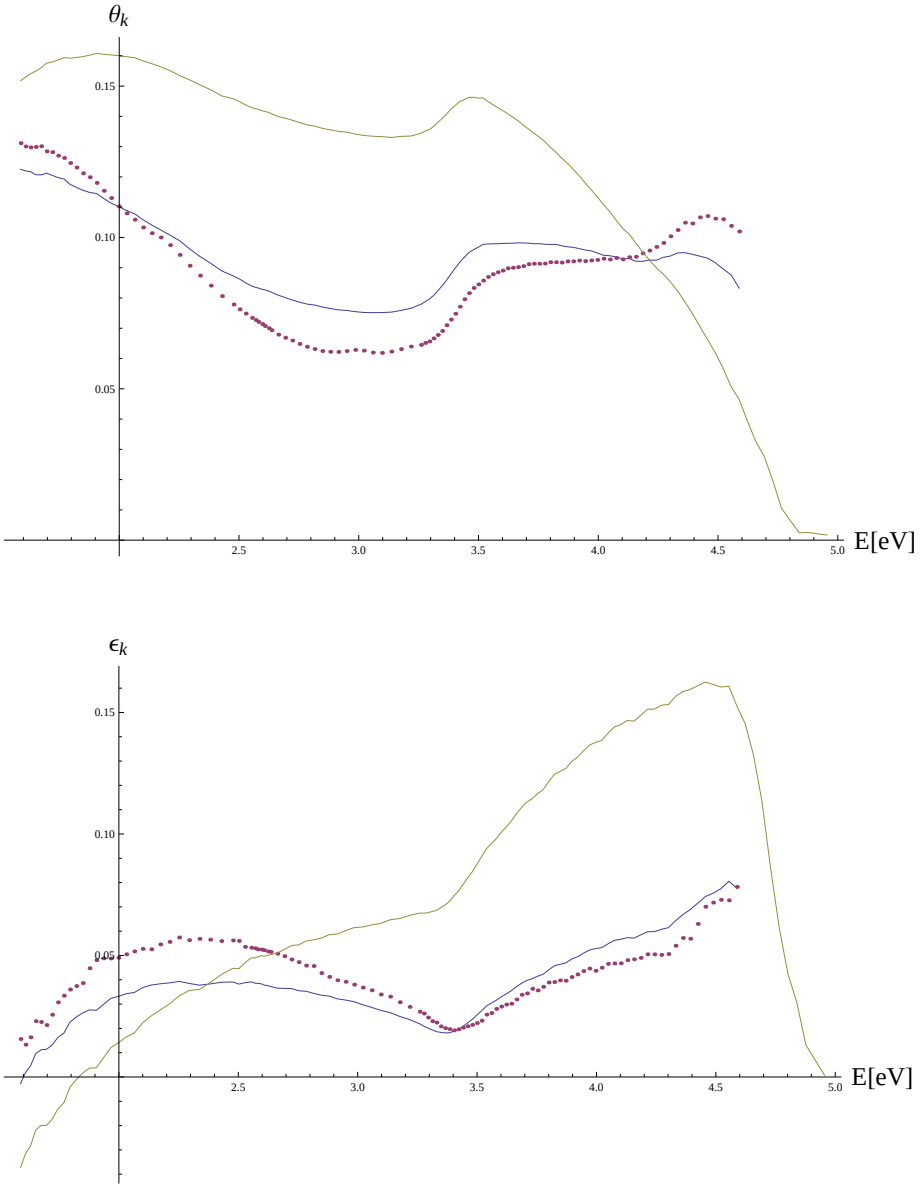

Figure 4.8: Kerr rotation (θ_k) and ellipticity (ϵ_k) as a function of light energy for the data from the AFM measurements. Dots represent the experimental results while the continuous lines represent the theoretical predictions; blue represents the results from the standard model while khaki represents the simpler model with the planar surfaces.

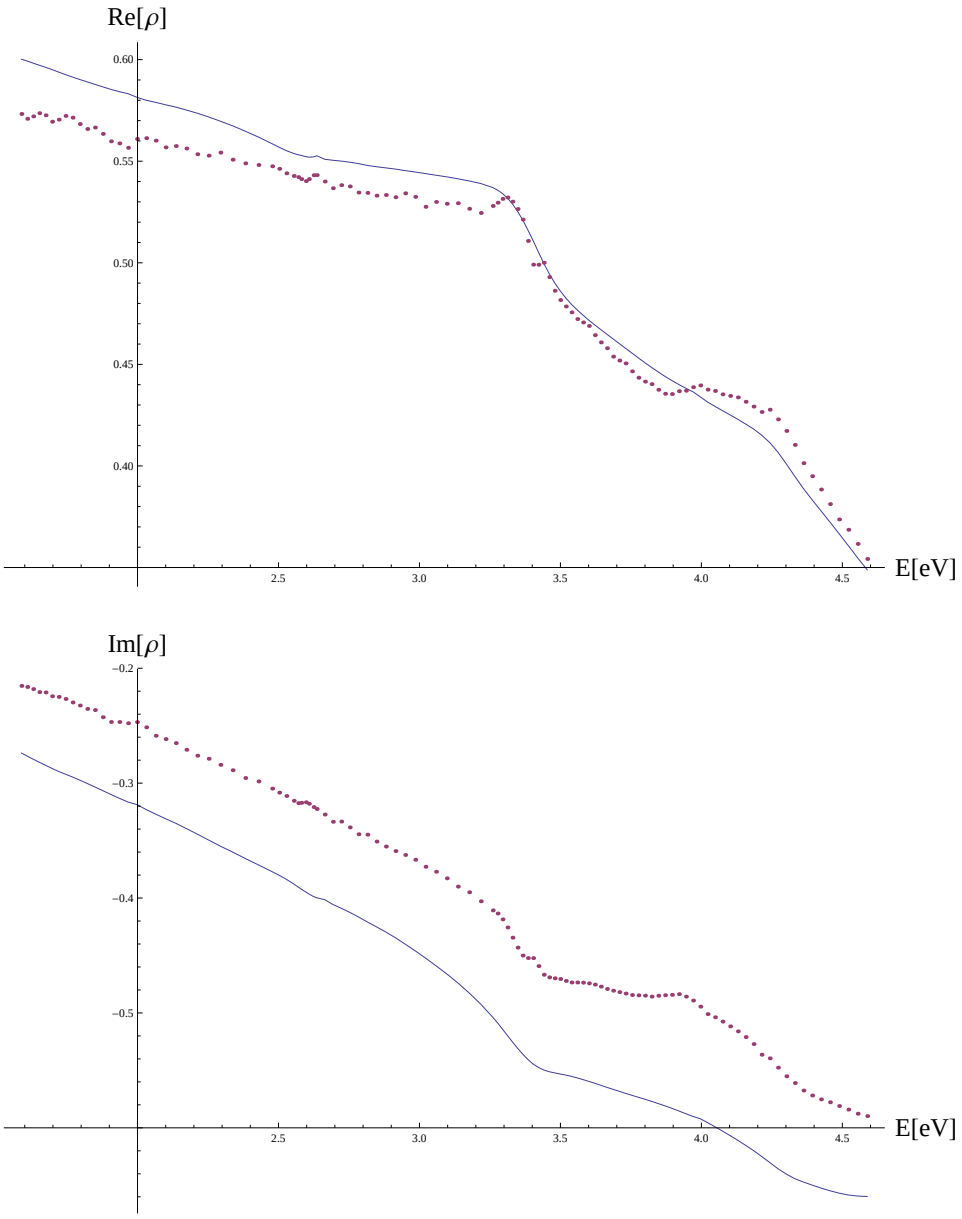

Figure 4.9: Quantity ρ as a function of energy (E) for the factory data. Dots represent the experimental results while the continuous lines represent the theoretical predictions.

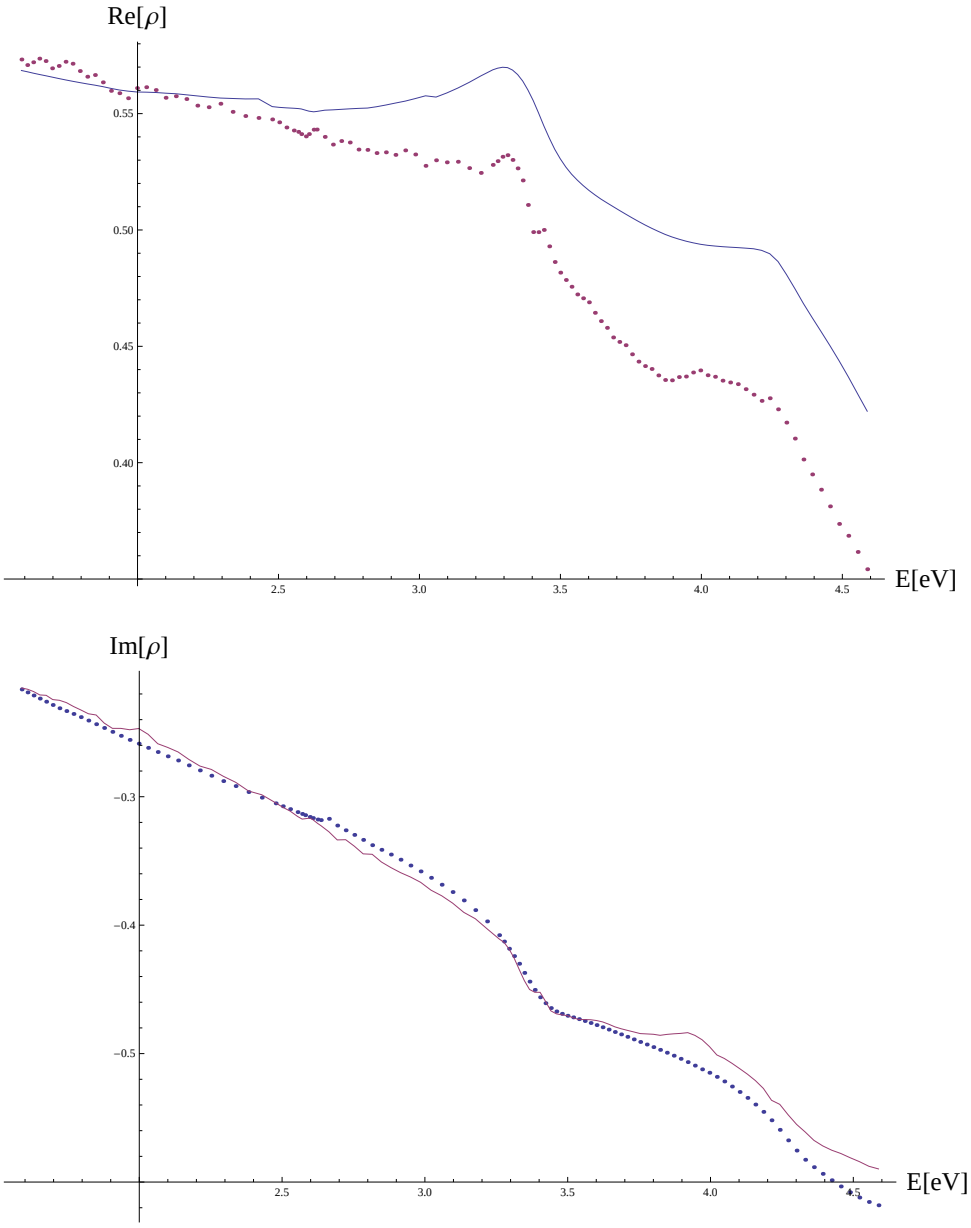

Figure 4.10: Quantity ρ as a function of energy (E) for the data from the AFM measurements. Dots represent the experimental results while the continuous lines represent the theoretical predictions.

Chapter 5

Conclusion

The primary purpose of this thesis was to create a model of diffraction gratings which makes it possible to compare experimental results (ellipsometric and magnetooptical) of our permalloy grating. Taking into consideration the fact that there were two sets of grating parameters availible - the factory data and the data from the AFM measurements - from the results we can conclude that the AFM measurements describe the grating more accurately than the factory data.

As the model is able to treat a fairly wide array of problems, we were able to test the it for the special case of the Fabry-Perot etalon in which comparison with a simpler method implies that the model yields the correct results for that special case.

Also, we were able to create a simple approximation of light trapping in solar cells and prove that a correctly chosen configuration can increase the absorption of light in solar cells.

Bibliography

[1] Masud Mansuripur. *Classical optics and its applications*. Cambridge University Press, 2002.

[2] Erwin G Loewen and Evgeny Popov. *Diffraction gratings and applications*, volume 58. CRC Press, 1997.

[3] https://i.ytimg.com/vi/Q0qrU4nprB0/0.jpg.

[4] Štefan Višňovskỳ. *Optics in magnetic multilayers and nanostructures*, volume 108. CRC Press, 2006.

[5] http://www.wolfram.com/mathematica/.

[6] Eugene Hecht. Optics 4th, 2002.

[7] Marius Peters, Marc Rüdiger, Hubert Hauser, Martin Hermle, and Benedikt Bläsi. Diffractive gratings for crystalline silicon solar cells-optimum parameters and loss mechanisms. *Progress in Photovoltaics: Research and Applications*, 20(7):862–873, 2012.

[8] RMA Azzam, NM Bashara, and Stanley S Ballard. *Ellipsometry and Polarized Light*. North Holland, 1978.

[9] Martin Veis and Roman Antos. Advances in optical and magnetooptical scatterometry of periodically ordered nanostructured arrays. *Journal of Nanomaterials*, 2013:3, 2013.

[10] Miroslav Nyvlt. *Optical interactions in ultrathin magnetic film structures*. PhD thesis, PhD. dissertation, Charles University, Prague, 1996.

List of Tables